Journal of Alloys and Compounds 676 (2016) 591–600

Contents lists available at ScienceDirect

Journal of Alloys and Compounds

journal homepage: http://www.elsevier.com/locate/jalcom

Strain induced phase formation, microstructural evolution and bandgap narrowing in strained TiO_2 nanocrystals grown by ball milling

Gone Rajender [a], P.K. Giri [a, b, *]

[a] Department of Physics, Indian Institute of Technology Guwahati, Guwahati 781039, India
[b] Centre for Nanotechnology, Indian Institute of Technology Guwahati, Guwahati 781039, India

ARTICLE INFO

Article history:
Received 24 November 2015
Received in revised form
16 March 2016
Accepted 21 March 2016
Available online 22 March 2016

Keywords:
TiO_2 nanocrystals
Strain
Williamson-Hall plot
Phase formation
Band gap engineering

ABSTRACT

Band gap narrowing in metal oxide semiconductor nanostructures is important and advantageous for various potential applications including visible light photocatalysis. We present a systematic study on the anomalous strain evolution, phase change and band gap narrowing in TiO_2 nanocrystals (NCs) as a result of ball milling. In addition to the size reduction and strain evolution with milling time, we report the formation of a new phase of TiO_2 with milling, as identified in the XRD pattern and Raman spectra for the first time. Besides the tetragonal anatase phase of TiO_2 NCs, two additional peaks centered at $2\theta = 31.28^\circ$ and 41.60° evolve with milling, and it corresponds to the $(\bar{1}\ 12)$ and (312) planes of Ti_3O_5, respectively. Further, our results show that the band gap of TiO_2 NCs reduces with increasing strain and lowest band gap achieved in strained TiO_2 is 2.71 eV, consistent with a recent theoretical calculation. The evolution of the crystallite size, strain, stress and energy density was evaluated from the line shape analysis of the XRD pattern using various models, such as uniform deformation model, uniform stress deformation model, uniform deformation energy density model and the results are compared with those obtained directly from HRTEM analyses. The increased d-spacing with milling time was attributed to the tensile strain in TiO_2 NCs. Direct evidence of lattice strain and strain relaxation is provided from HRTEM imaging and differential scanning calorimetry analyses. Our results demonstrate strain engineering of TiO_2 to achieve narrow bandgap in anatase TiO_2 NCs, which are promising for visible light photocatalytic and other emerging applications.

1. Introduction

Titanium oxide (TiO_2), an important wide band gap semiconductor, has been studied extensively in the past decades due to wide range of applications in photo catalysis, solar cells, fuel cells, chemical sensors, biomedical, lithium storage, glass coating, self-cleaning etc. [1–10] It is well known that the particle size and crystal morphology play an important role in photocatalytic, thermal and magnetic properties of TiO_2 [11–13]. The functional properties of TiO_2 are strongly dependent on its phase and microstructure [14–18]. Indeed, the crystallite size is critical for phase stability, and the presence of micro- and/or macro-strains may affect the photoinduced hydrophilicity [19]. The phase change of TiO_2 based compounds (Ti_3O_5, Ti_2O_3, Ti_4O_7) etc. plays an important role for various applications, like heat storage, sensors [20]. Among these polymorphs, Ti_3O_5 is one of the most promising material for optical memory applications [21]. Many synthesis techniques have established for controlled synthesis of TiO_2 nanocrystals (NCs), such as hydrothermal [22], sol-gel [14], sonochemical and microwave [16], microemulsion-mediated hydrothermal [18], wet chemical [23] methods etc. Among these techniques, ball milling is a simple and low cost technique without involving any complex chemical synthesis.

Several groups reported the evolution of strain with size reduction in NCs of different semiconductors, such as Si NCs [24], Ge NCs [25] and ZnO NCs etc. [26–28] However, only a few reports investigated on the role of strain and size induced broadening of XRD peaks in TiO_2 NCs [29]. Recently, Ansari et al. reported the gold and silver plasmonic nanoparticles mediated band gap engineering

* Corresponding author. Department of Physics, Indian Institute of Technology Guwahati, Guwahati 781039, India.
E-mail address: giri@iitg.ernet.in (P.K. Giri).

http://dx.doi.org/10.1016/j.jallcom.2016.03.154
0925-8388/

in TiO_2 [30,31]. Tripathi et al. reported the temperature dependent variation of strain in TiO_2 NCs [32]. The strain analysis has been mostly limited to Williamson-Hall (W–H) method. However, an extensive analysis of the X-ray diffraction (XRD) data by means of fitting of line shape with various models has not been reported earlier. Besides the size and strain, the band gap plays the leading role to tune the optoelectronic properties. Bulk TiO_2 band gap falls in the UV region, thus it limits the use in optoelectronic and visible light photocatalysis. Unfortunately, no experimental report is available on the band gap modification of TiO_2 NCs by strain engineering, while only theoretical report [33] is available on band gap reduction using strain. Denis et al. [34] reported that strain is created in bulk TiO_2 surface by Ar ion bombardment, but its influence on the band gap evolution was not studied. Here, we demonstrate the band gap tuning by strain engineering with a simple ball milling approach. This is very useful for photocatalytic and optoelectronics applications of TiO_2. To the best of our knowledge, no experimental report is available on band gap modification of TiO_2 using simple ball milling technique. The anomalous strain behaviour reported here has not been addressed earlier in the literature.

Generally, for the small NCs the XRD pattern is different from its bulk crystalline counterpart. The deviation from perfect crystalline order leads to a broadening of the diffraction peaks. It is known that the mechanical alloying may induce a large amount of strain in the powders [35]. XRD line profile analysis is a simple and powerful tool to estimate the crystalline size and lattice strain [36]. Out of different available methods to estimate the crystallite size and lattice strain, the W-H analysis, pseudoVoigt function, Rietveld refinement, and Warren Averbach analysis are mostly common [37–39]. W-H analysis is a simplified integral breadth method where both size-induced and strain-induced broadenings are investigated by considering the peak width as a function of 2θ [27]. To the best of our knowledge, band gap modification by strain and modified W-H method has not been discussed extensively for the calculation of size and strain in TiO_2 NCs.

In the present work, we have grown TiO_2 NCs of sizes down to 11 nm by simple ball milling method. As a result of milling, a new phase of TiO_2 is reported for the first time. The particle size and strain are calculated in a systematic way by means of XRD analysis and direct imaging i.e. by transmission electron microscopy (TEM). Different models are utilized to calculate crystallite size and strain from XRD line profile and the correlation between the different models are made for different parameters. The band gap modification achieved with the combined effect of strain and oxygen vacancy defects in TiO_2 NCs has been explored in detail. In addition to the XRD, the phase change and nature of strain are further confirmed from the Raman spectroscopy. Finally, the strain relaxation and structural changes are further investigated by DSC measurements.

2. Experimental details

TiO_2 NCs are prepared from commercially available TiO_2 powder with initial average particle size ~80 nm (>99% purity) using mechanical ball milling method. Ball-milling was performed at 350 rpm for the duration up to 40 h in a ZrO_2 vial (Restch, PM100) under ambient condition. Small ZrO_2 balls (diameter 5 mm) were used for the ball-milling and this ensured contamination-free milling process. The ball to powder weight ratio was taken as 10:1. The milled samples were collected at 4, 8, 12, 16, 20, 30 and 40 h duration. Very fine TiO_2 NCs with few nanometer sizes were obtained after milling. For the convenience of subsequent discussion, we denoted the unmilled, 4 h, 8 h, 12 h, 16 h, 20 h, 30 h and 40 h milled TiO_2 NCs samples as T0h, T4 h, T8 h, T12 h, T16 h, T20 h, T30 h, and T40 h, respectively. Post growth annealing experiment was conducted at 350 °C for 90 min using a quartz tube mounted inside a muffle furnace, in air atmosphere. Note that the 16 h milled annealed sample is named as T16 hA.

3. Characterizations

XRD pattern is obtained with Rigaku RINT 2500 TTRAX-III using Cu K_α radiation at the operating voltage 50 kV and current 180 mA. For careful determination of average nanocrystals size, internal lattice strain, and, energy density, XRD data was collected at a slow scan rate of 0.002° per second. For the diffraction peak of (101) planes, all the samples were scanned in the range 23–27 (2θ) with a very slow scan rate of 0.0005° per second. Particle size analysis, high magnification surface morphologies, crystallinity and lattice spacing of the samples were studied with transmission electron microscopy (TEM), high resolution TEM (HRTEM) and selected area electron diffraction (SAED) patterns (JEOL-JEM 2010 operated at 200 kV). Specimens for HRTEM investigations were prepared by dispersing powder particles in ethanol and drop casting them onto the Cu grid of 400 meshes (Pacific Grid, USA). Raman analysis of the samples was performed in Raman spectrometer (Horiba, LabRam HR) with excitation wavelength 514.5 nm. In order to avoid the laser heating induced Raman shift, we have performed the Raman measurements at very low laser power (0.9 mW). The UV-visible diffuse reflectance spectroscopy (DRS) measurements were performed using a commercial spectrophotometer equipped with integrating sphere (PerkinEmler, UV win Lab). To study the strain relaxation and structural changes, the DSC/TGA measurements were performed in STA 449 F3 Jupiter DSC analyser (Netzsch, Germany) with high temperature tungsten furnace (1700 °C) with heating rate of 5 °C/min by purging the high purity Ar gas. Details of the photoluminescence and photocatalysis experiment are provided in the Supporting information, SI-1.

4. Results and discussion

4.1. XRD analysis

Fig. 1(a) shows the comparison of the XRD pattern of different TiO_2 NCs grown by ball milling along with the unmilled TiO_2 powder, while Fig. 1(b) shows a magnified view of the comparison of XRD pattern of all the samples in range ($2\theta = 24–26°$). Inset of Fig. 1(b) represents the shift in XRD peak for T16 h sample before and after annealing. The plotted curves are vertically shifted for clarity. All the peaks labelled in Fig. 1(a) correspond to the anatase phase of TiO_2. Two new peaks appear after 4hr milling and become prominent for the higher milling time (indicated by "*" in Fig 1(a)). Note that, these peaks were not seen in case of unmilled sample. For the size and strain calculations, all XRD peaks were fitted with Gaussian line shape to determine the precise peak position and full width at half maximum (FWHM) of the peaks. From the fitted parameters, it was observed that the FWHM of the peaks gradually increases with increasing milling time. This broadening confirmed the size reduction and the development of strain in the TiO_2 NCs [26,40]. In addition to the peak broadening, we also observed a shift in the peak position. The peak shift after milling might be due to different kinds of strain (tensile and compressive) developed in the TiO_2 NCs. The fitted parameters (peak centre and FWHM) of (101) peak of all the samples are shown in Table 1. It is clear that the peak centres are shifted towards lower 2θ values with increasing milling time up to 16 h and it indicates the presence of the tensile strain in the NCs. Note that the T16 h sample shows the highest peak shift as compared to the other samples. With further increase of milling time, the peak centres are shifted towards higher 2θ value as

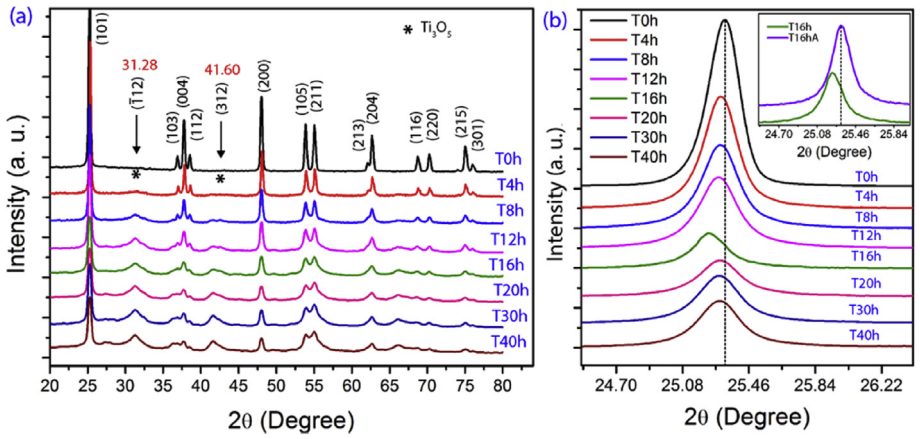

Fig. 1. (a) Comparison of the XRD pattern of ball milled TiO_2 powders for different milling times (T0 h to T40 h). The arrows indicate the peaks due to a new phase Ti_3O_5. (b) Slow scan XRD pattern of (101) peak of ball milled TiO_2 NCs. Inset shows shift in the XRD peak for T16 h before and after annealing. The curves are vertically shifted for better clarity.

Table 1
Gaussian line shape fitted parameters for the XRD pattern for (100) peak of different samples.

Sample	Peak centre in (Degree)	FWHM in (Degree)
T0h	25.315	0.216
T4h	25.296	0.238
T8h	25.294	0.269
T12 h	25.283	0.292
T16 h	25.203	0.319
T16 hA	25.320	0.243
T20 h	25.285	0.321
T30 h	25.288	0.325
T40 h	25.289	0.354

compared to that of T16 h (see Fig. 1(b) and Table 1). Thus, it is found that the tensile strain reaches its maximum value for milling time of 16 h and further milling causes reduction of tensile strain or strain relaxation. To ascertain the strain contribution in the broadening and peak shift, the maximum strained sample (T16 h) is annealed in air atmosphere at 350 °C for 90 min (sample named as T16 hA). Interestingly, the peak centre of T16 hA sample shifts to the higher 2θ value and it closely matches with the pristine sample (T0h) (see inset of Fig. 1(b)). Note that the peak broadening is also reduced after annealing. Thus the presence of strain in TiO_2 NCs is confirmed from the annealing experiment and the strain relaxation happens after annealing of T16 h. Interestingly, in addition to the anatase phase of pristine TiO_2, we observed two new peaks at 2θ~31.28° and 41.6° after milling, which correspond to the ($\bar{1}$ 12) and (312) planes of Ti_3O_5 (JCPDS No. 74-0819), respectively (see Fig. 1(a)). It is clear that with increasing milling time, besides the size reduction, the mechanical milling induces phase change in TiO_2, as evident from the new peaks (marked with "*") shown in the XRD pattern in Fig. 1(a). This is consistent with a recent report [41]. This phase change is attributed either to the high-pressure and high-temperature generated locally in the TiO_2 powder or to the high temperatures (the so-called hot spots) produced during the ball milling process [41]. Note that Ti_3O_5 is an oxygen deficient phase of TiO_2, which evolves during the milling in air ambient. The oxygen deficiency gives rise to oxygen vacancy defects in TiO_2 and presence of oxygen vacancy (O_v) defects in milled TiO_2 powers is confirmed from the photoluminescence (PL) studies, which shows strong visible PL after milling (Fig. S1, Supporting Information). It is well known that visible PL in TiO_2 arises from the O_v defects in TiO_2 [42]. We have noticed that T16 hA sample does not show any significant change in phase after annealing (data not shown). It is believed that 350 °C annealing is not significant for phase change to occur. However, at higher temperature (>620 °C), the anatase phase changed to the rutile phase [43]. Generally, the FWHM of the Bragg peak is contributed by a combination of both instrumental broadening and sample dependent FWHM. To estimate the actual sample broadening, it is necessary to subtract the instrumental broadening.

4.2. Particle size and strain analysis

4.2.1. Scherrer method

XRD pattern can be utilized to evaluate the broadening of peaks with reduction in crystalline size and lattice strain. If the strain contribution is ignored, the particle size can be estimated from the well-known Scherrer Equation [28]:

$$D = \frac{K\lambda}{\beta_D COS\theta} \tag{1}$$

$$\cos\theta = \left(\frac{1}{\beta_D}\right)\cdot\frac{K\lambda}{D}$$

where K is a constant equal to 0.94 for spherical shaped particles, D is the crystallie size in nm, λ is the wavelength of the x-ray (1.54056 Å for Cu K_α radiation), β_D is the FWHM in radian and θ is the peak centre. 1/β is plotted as a function of cosθ and by straight line fitting of the data, the crystallite size D was extracted from the slope of the fitted line. Calculated values of crystallite sizes from Scherrer method are tabulated in Table 2. It is observed from Table 2 that the particle size decreases with increasing milling time, as expected. The particle size calculated for T0h, T16 h and T40 h samples are ~78, ~60 and ~17 nm, respectively. Note that the average particle sizes calculated from the TEM images for these samples are ~80, ~65 and ~10 nm, respectively. The discrepancy in the size estimation, particularly at higher milling time, may be due the exclusion of strain contribution in Scherrer equation. A better estimation of size and strain can be made from W-H method discussed below.

4.2.2. W-H methods

a. Uniform deformation model. The strain-induced broadening arising from crystal imperfections and distortion is expressed as:

$$\varepsilon = \frac{\beta_{hkl}}{4\,tan\theta} \tag{2}$$

Table 2
Summary of calculated parameters such as average nanocrystallite size (D), strain (ε), stress (σ), energy density (U) obtained from various models and TEM analysis.

Sample name	Scherrer method	Williamson-Hall method									TEM method	
		UDM		USDM			UDEDM					
	~D (nm)	~D (nm)	ε (%)	~D (nm)	ε (%)	σ(MPa)	~D (nm)	ε (%)	σ (MPa)	U (kJ/m^3)	~D (nm)	ε (%)
T0h	78	72	0.20	76	0.21	259.64	77	0.19	242.28	232.17	80	–
T12 h	69	66	0.62	67	0.37	468.09	65	0.36	469.43	859.64	59	
T16 h	60	58	0.79	59	0.51	631.57	55	0.50	603.38	1512	65	2.11
T16 hA	63	60	0.26	–	–	–	–	–	–	–	–	
T20 h	54	50	0.55	51	0.42	535.84	45	0.43	550.81	1188.1	49	
T30 h	28	26	0.47	25	0.31	433.55	24	0.34	493.09	849.49	24	
T40 h	17	10	0.36	9	0.27	350.81	10	0.25	316.59	397.96	11	1.54

The W-H method does not follow a $1/\cos\theta$ dependency as in the Scherrer Eq., but instead varies with $\tan\theta$. This fundamental difference allows for a separation of broadening when both small crystalline size and micro-strain occur together. This difference in approaches presented in the following assume that size and strain broadening are additive components of the total integral breadth of FWHM of a Bragg peak [44]. The distinct θ dependences of both effects laid the basis for the separation of size and strain broadening in the analysis of W-H. Then the observed FWHM is the sum of Eqs. (1) and (2)

$$\beta_{hkl} = \frac{K\lambda}{D\cos\theta} + 4\varepsilon\tan\theta$$

By rearranging,

$$\beta_{hkl}\cos\theta = \frac{K\lambda}{D} + 4\varepsilon\sin\theta \quad (3)$$

Eq. (3) represents the uniform deformation model (UDM), where the strain is assumed to be uniform in all crystallographic directions, thus considering the isotropic nature of the crystal, where all the material properties are independent of the direction along which they are measured. A plot drawn between 4sinθ versus $\beta_{hkl}\cos\theta$ allows the determination of strain and crystallite size from the slope and intercept, respectively. Fig. 2(a)-(f) represents the UDM fitted graphs of 0 h, 12 h, 16 h, 20 h, 30 h and 40 h milled TiO_2 NCs, respectively. The experimental data points are shown with symbols and fitted data points are shown with straight line. The UDM fitting parameters are tabulated in Table 2. From Table 2, we observe that the microstrain gradually increases with increasing milling time and gets saturated for an intermediate milling time and then again decreases for higher milling time (up to 40 h). This is consistent with the reported literature for other semiconductors, e.g. Si NCs [24]. On the other hand, the particle size systematically decreases with increasing milling time and it reaches a value of ~10 nm for 40 h milling, which is quite consistent with HRTEM analysis. Note that the UDM model assumes an isotropic nature of

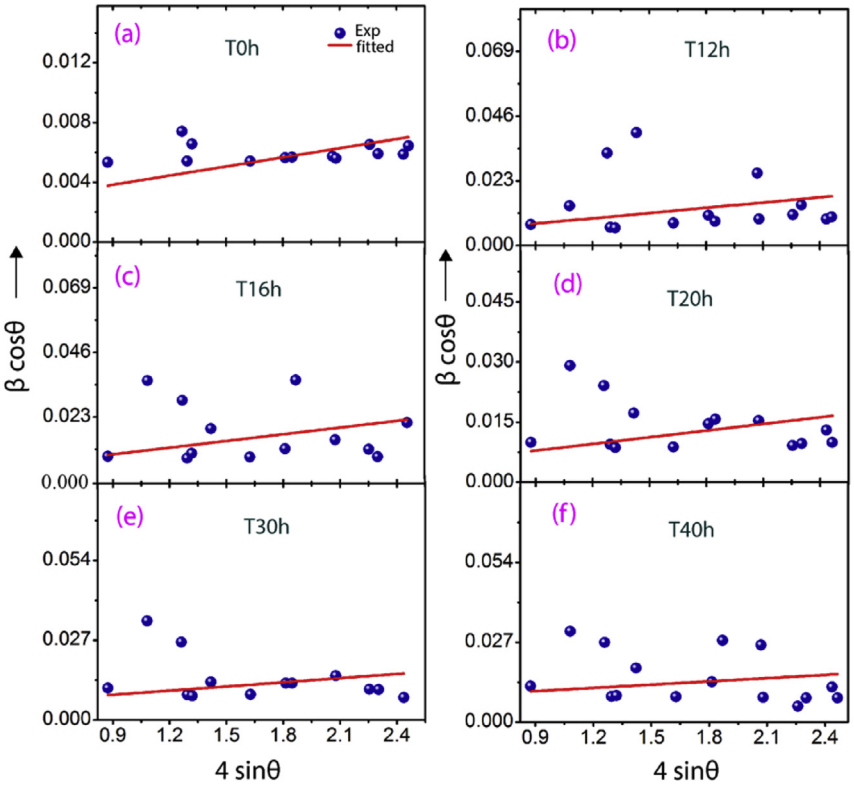

Fig. 2. (a–f) UDM fitting of XRD data for TiO_2 NCs obtained after 0 h, 12 h, 16 h, 20 h, 30 h, and 40 h milling, respectively. The experimental data are shown with symbols and fitted data are shown with solid line.

the crystal, which is not very realistic.

b. Uniform stress deformation model (USDM). Here the uniform deformation stress and uniform deformation energy density were taken into account; the anisotropic nature of Young's modulus of the crystal is more realistic. The generalized Hook's law refers to the strain, keeping only the linear proportionality between the stress and strain, i.e., $\sigma = \varepsilon Y$. Here, the stress is proportional to the strain, with the constant of proportionality being the modulus of elasticity or Young's modulus, denoted by Y. In this approach, the W-H equation is modified by substituting the value of "ε" in Eq. (3);we get,

$$\beta_{hkl}cos\theta = \frac{K\lambda}{D} + \frac{4\sigma sin\theta}{Y_{hkl}} \tag{4}$$

Y_{hkl} is Young's modulus in the direction perpendicular to the set of the crystal plane (hkl). For a given tetragonal crystal, Young's modulus is given by the following relation [45].

$$\frac{1}{Y_{hkl}} = \frac{s_{11}(h^4+k^4)+(2s_{12}+s_{66})h^2k^2+(2s_{13}+s_{44})(h^2+k^2)l^2+s_{33}l^4}{(h^2+k^2+l^2)^2} \tag{5}$$

Where s_{11}, s_{12}, s_{13}, s_{33}, s_{44}, and s_{66} are the elastic compliances of anatase TiO_2, and their values are 5.1×10^{-12}, -0.8×10^{-12}, -3.3×10^{-12}, 10.7×10^{-12}, 18.5×10^{-12}, and 16.7×10^{-12} m^2 N^{-1}, respectively. However, for the anatase phase, only theoretical elastic constant values are available in the literature [46]. Plots were made for $(4\sin\theta)/Y_{hkl}$ vs. $\beta_{hkl}\cos\theta$ for all the peaks in a sample and this process was repeated for different samples. The slope of the fitted line gives the stress and the intercept yields the crystallite size for each case. Then, we can calculate the strain from the linear relation between stress and strain $\sigma = \varepsilon Y$. Fig. 3(a-f) illustrates the USDM fitted curves of 0 h, 12 h, 16 h, 20 h, 30 h and 40 h milled TiO_2 NCs, respectively. The experimental data points are shown with symbols and the fitted data points are shown with straight line. In this model, again the strain increases with increasing milling time, saturated after 16 h milling and then reduces further milling time. At the same time, particle size systematically decreases with increasing milling time. The fitted results are shown in Table 2. Note that the particle size obtained in this model is quite close to that obtained from the UDM model, while the strain values are quite different in these two models. Considering the more realistic nature of this model, the obtained D and ε values are considered to be more reliable in USDM.

c. Uniform deformation energy density model (UDEDM). This model can be used to determine the deformation energy density, particle size, stress and strain parameters. In Eq. (4), the crystals are assumed to have a homogeneous and isotropic nature. However, in many cases, the assumption is not valid. Moreover, the constants of proportionality associated with the stress-strain relation are no longer independent when the strain energy density u is considered. For an elastic system that follows Hooke's law, the energy density u (energy per unit volume) can be calculated from $u = (\varepsilon^2 Y_{hkl})/2$. Then Eq. (3) becomes,

$$\beta_{hkl}cos\theta\frac{K\lambda}{D} + \left(4sin\theta\left(\frac{2u}{Y_{hkl}}\right)^{\frac{1}{2}}\right) \tag{6}$$

Eq. (6) represents the USDEM. The uniform deformation energy density can be calculated from the slope of the line plotted between $\beta_{hkl}\cos\theta$ and $4\sin\theta(2/Y_{hkl})^{1/2}$. The crystallite size is calculated from the y-intercept. Using the relation $\sigma = \varepsilon Y$ *and* $u = (\sigma^2/2Y_{hkl})$, we can calculate the stress and strain on the TiO_2 NCs. Fig. 4(a-f)

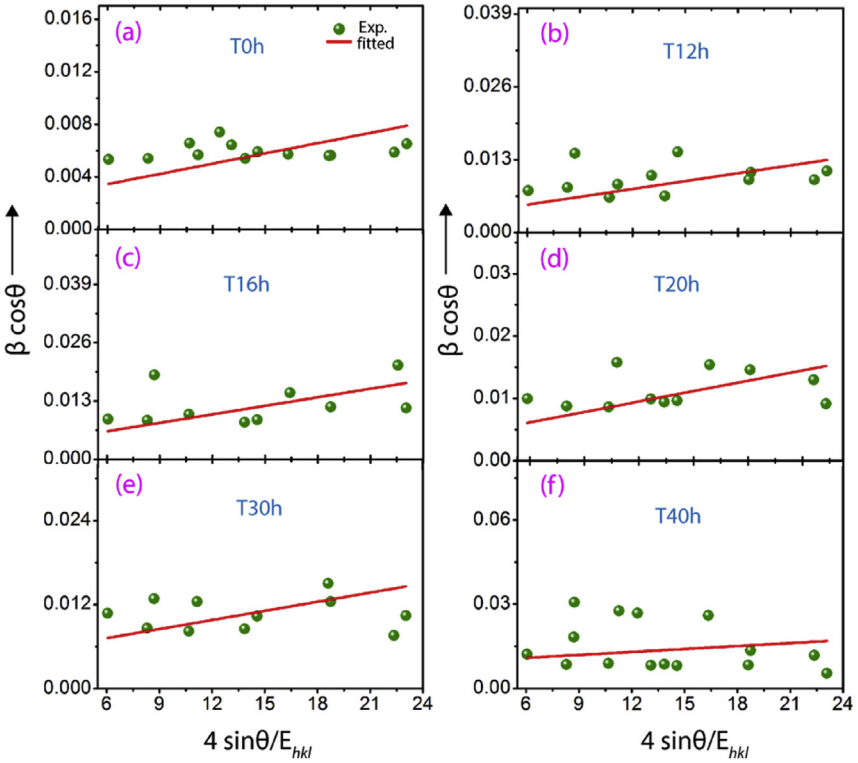

Fig. 3. (a–f) USDM model fitting for samples T0h, T12 h, T16 h, T20 h, T30 h, and T40 h, respectively. The experimental data are shown with symbols and the fitted data are shown with line.

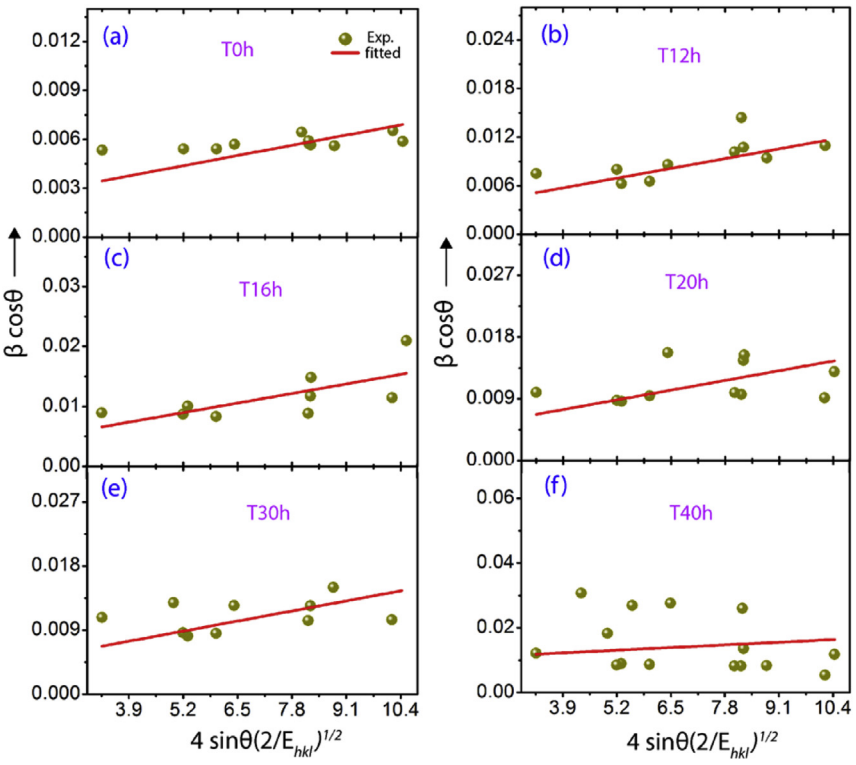

Fig. 4. (a–f) The UDEDM fitting of XRD data for T0h, T12 h, T16 h, T 20 h, T30 h, and T40 h, respectively. The experimental data are shown with symbols and the fitted data are shown with line.

represents the UDEDM fitted graphs for 0 h, 12 h, 16 h, 20 h, 30 h and 40 h milled TiO_2 NCs respectively. The experimental data points are shown with symbols and the fitted data is shown with a straight line. The calculated parameters from this model are tabulated in Table 2. This method also concludes that the particle size decreases with increasing milling time. The strain values of T0h, T16 h and T40 h samples are 0.2%, 0.5% and 0.25% respectively. The strain values obtained for these samples using the above models (USDM and UDEDM) are fully consistent. However, the strain values obtained from HRTEM analysis is relatively higher (see Table 2). The mismatch may be due to the fact that XRD analysis yields average strain, where the strain calculated from HRTEM is only for a particular plane and for a few particles.

d. Comparison of size and strain from different models. Fig. 5(a-c) represents a comparison of particle size and strain as a function of milling time for different models, i.e. UDM, USDM, and UDEDM. It is observed that in all the models, the size systematically decreases with increasing milling time from 0 to 40 h. However, the strain first increases with milling time up to 16 h milling and then decreases with further milling. Up to 16 h milling, the strain developed is tensile in nature, and then the strain reduces for further milling perhaps due to the strain relaxation by formation of dislocations. Note that for all models, the strain value is of the order of 10^{-2} indicating the consistency of UDM, USDM and UDEDM models.

4.3. Direct evidence of strain from HRTEM

TEM is an important tool to estimate the size and shape of the NCs. Fig. 6 represents the size and lattice spacing of TiO_2 NCs for different milling times. Fig 6(a), (c) and (e) are the TEM images of T0h, T16 h and T40 h samples and (b), (d) and (f) are the corresponding HRTEM images (after IFFT). The inset of Fig. 6(f) (right lower corner) shows the selected area electron diffraction (SAED) pattern of T40 h sample indicating the tetragonal crystal phase of NCs. The strained portions are marked by oval ring for the T40 h sample (Fig. 6(f)). Note that the lattice strain is very high for T16 h as evident from Fig 6(d). The NCs size distribution of the T40 h is shown in Fig. 6(e) as an inset. The average particle size and lattice spacing corresponding to (101) planes of T0h sample is ~80 nm and 3.24 Å, respectively. The lattice spacing of T16 h sample corresponding to the (101) planes is 3.31 Å, which is much higher than that of T0h. The higher d-spacing confirms the tensile strain in the lattice, which is fully consistent with the lower 2θ peak shown in the XRD pattern. It is evident from the HRTEM image (see Fig. 6(d)) that the lattice fringes are quite distorted at many locations due the high strain. This may be due to dislocations in TiO_2 NCs created by the ball milling. The strain calculated for T16 h sample using the HRTEM analysis is 2.16%, which is higher than the strain calculated from UDM, USDM, and UDEDM models (see Table 2). In addition to the distortion of lattice fringes, some changes in the surface morphology are also observed in T16 h sample. The surface of the NCs looks ruptured due the high strain. Thus, the strain creates some morphological disorder in the sample. This is observed particularly for T16 h sample because these NCs are highly strained during milling. On the other hand, the morphological features of NCs in T0h and T40 h samples are almost spherical in nature without distortion of edges (see Fig. 6(a, e)). Further, the lattice spacing calculated for T40 h sample is 3.29 Å, a little lower than that of the T16 h sample, consistent with the XRD analysis. The strain associated with the NCs is 1.54%, again higher than that the strain calculated from the above models (see Table 2). These results are consistent with the XRD results, where 2θ value shifted to a higher angle. FESEM morphology images for T4 h and T12 h are given in Fig. S2(a,b) and the TEM images for the T20 h and T30 h are provided in Figure S2(c, d) (Supporting Information). Note that the

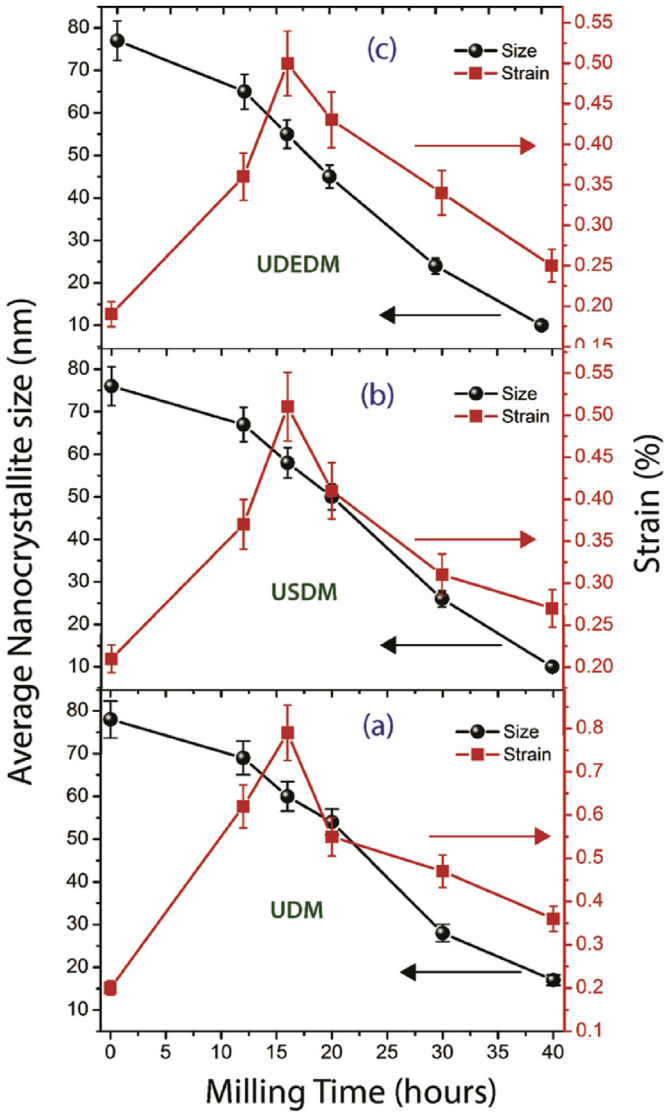

Fig. 5. Comparison of the average nanocrystallite size and strain in TiO_2 NCs as a function of milling time calculated by (a) UDM, (b) USDM and (c) UDEDM methods.

sizes measured from TEM analysis closely matches with that found from the XRD line shape analysis.

4.4. Evolution of strain and defects from Raman spectra

For further confirmation of the particle size reduction, strain evolution and defects on the band gap modification of TiO_2 NCs, Raman measurement was performed. Raman spectroscopy is an excellent tool to investigate the strain, phonon confinement, and stoichiometry defects in TiO_2 NCs based on shifting and broadening of spectral lines. Fig. 7(a) represents the Raman spectra of T0h, T4 h, T16 h, and T40 h samples and inset shows the zoomed view of the spectra in the range 220–700 cm^{-1} for comparison. All the vibrational modes corresponding to anatase phase of TiO_2 are present here and it is consistent with the literature [47–50]. Along with the characteristics anatase phase of TiO_2, some new spectral features are found in different milled samples (see inset of Fig. 7(a)). Fig. 7(b) shows a comparison of E_{1g} mode for T0h, T16 h and T40 h samples and inset shows the change in the peak profile for 16 h sample before and after annealing. It is clear from Fig. 7(a) that the new peaks started appearing after 4 h milling and intensity of these peaks increased with increasing milling time. Note that the formation of new phase after 4 h milling is also seen from XRD data. However, XRD pattern reveals only the Ti_3O_5 phase. On the other hand, Raman spectra distinguish the type of phase of Ti_3O_5. It is believed that the new peaks correspond to β- Ti_3O_5 phase. Similar results were reported by Wu et al. [51] and Hamouda et al. [52] Note that β-Ti_3O_5 has 24 Raman active vibrational modes ($16A_g + 8B_g$). However, some of the spectral lines are very weak in intensity. Consequently, only the strong Raman peaks (centered at ~170, ~316, ~340, ~360, and ~427 cm^{-1}) have been observed. It may indicate that only a small fraction of the sample contains β- Ti_3O_5 as confirmed from the XRD analysis. Although, several peaks are observed in milled TiO_2 NCs, the most intense peak (E_{1g}) at ~143–145 cm^{-1} is significant. A closer analysis of E_{1g} mode reveals the influence of strain and phonon confinement on the line shape [53] and oxygen related stoichiometry defects [54]. The influence of strain on the other Raman modes of TiO_2 NCs with anatase phase was relatively poor [55]. Most importantly, broadening of Raman modes implies the reduction of nano crystalline size and shift in Raman frequency, implying tensile or compressive strain depending upon the red shift or blue shift, respectively. The competing effects of the phonon confinement and strain on the Raman spectrum can make the analysis difficult for TiO_2 NCs. Note that the TiO_2 nanocrystallites of sizes under 10 nm usually influence the Raman spectra through phonon confinement effect [53,55,56]. In the present case, we have obtained TiO_2 NCs of size ≥10 nm for different milled sample (T40 h). Thus, the phonon confinement effect may not be significant in our samples. We believe that the broadening and shift of Raman peaks are mostly due to the strain and O_v defects caused by the milling process. The centre of the E_{1g} peak for T0h, T4 h and T16 h and T40 h are at 144.38, 143.91, 143.20 and 143.91 cm^{-1}, respectively. This peak shift is quite consistent with the XRD analysis, where we have found the tensile strain in our samples. The initial red shift of the peak positions are due to the tensile strain and the later blue shift is due the reduction of tensile strain for longer milling time. Similar observations were also reported in case semiconductor nanowires and CdSe quantum dots [57–59]. Further, the strain relaxation was confirmed from T16 hA sample. The peak centre of T16 hA shifts to higher wave number, compared to the T16 h sample (see inset of Fig. 7(b)) and attains the value of pristine sample (T0h). This is also consistent with the XRD analysis. Thus, the micro Raman analysis further augmented the nature of strain in the TiO_2 NCs, which is fully consistent with the XRD analysis.

4.5. Effect of strain on band gap reduction

The nature of strain and its effect on band gap tuning of anatase TiO_2 NCs was analysed by UV-visible DRS. It may be mentioned that the band gap tuning of bulk anatase TiO_2 has been possible mostly by doping/composite with other elements. The DRS data of ball milled samples (shown in Fig. S3, Supporting information) shows significant changes in the reflectance spectrum of TiO_2 NCs after ball milling. Fig. 8(a) shows the UV-vis absorption spectra obtained from the Kubelka-Munk function for T0h, T16 h and T40 h samples. The band gap is estimated from the UV–visible absorption edge (Kubelka-Munk function) [30] and the values are 3.14 eV for T0h, while T16 h and T40 h with high tensile strain show reduced band gaps of 2.71 and 2.79 eV, respectively. This reduction in band gap is very significant and it is believed to be caused primarily by the lattice strain in TiO_2 NCs, observed experimentally for the first time. Our results are consistent with the theoretical prediction of bandgap narrowing in anatase TiO_2 by applying strain along a soft crystal direction [33]. It has been argued that in anatase TiO_2, due to the layered structure with soft crystal direction perpendicular to the

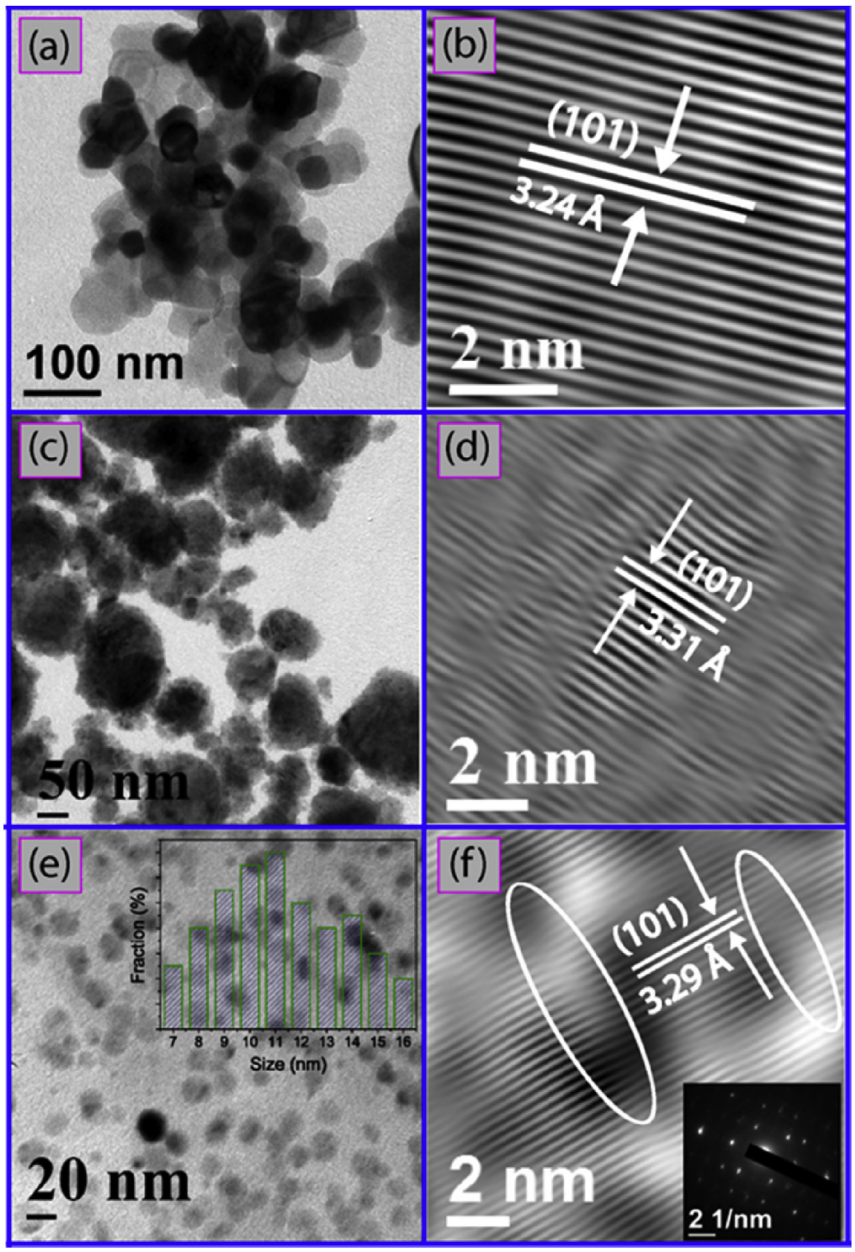

Fig. 6. (a, c, e) TEM images of T0h, T16 h and T40 h samples, and (b, d, f) corresponding HRTEM lattice images showing d-spacing of (101) planes, respectively. The inset in (e) shows the size distribution of TiO_2 NCs in T40 h sample. The inset in (f) shows the tetragonal phase of TiO_2 NCs in T16 h. The highly strained region of image in (f) is marked with oval shaped rings. In case of T16 h, lattice strain is highest (image d).

layer plane, its bandgap could be effectively reduced by applying stress along the soft crystal direction. In this case, ball milling produces strain in different crystal directions and soft direction will be affected most. We believe that the reduction in band gap achieved in this case is due to the combined effect of lattice strain and lattice defects induced by the ball milling. Since the achieved band gap of 2.71 eV falls in the visible region of spectrum, the ball milled TiO_2 would be suitable for visible light photocatalysis. Indeed, our preliminary results on the visible light photoctalysis studies show that the performance of ball milled TiO_2 NCs is better than the pristine TiO_2 NCs in the photocatalytic degradation of Methylene blue (Fig. S4, Supporting Information). Ball milled TiO_2 shows a degradation of ~52% as compared to only ~36% degradation in pristine TiO_2 NCs. Note that the optimization of defects is necessary for achieving efficient charge separation needed in photocatalysis process. In contrast to T16 h sample, the band gap of T40 h sample increases to 2.79 eV. Since the change of band gap follows the trend of the change in strain (tensile), the enhancement in band gap arises primarily from the tensile strain in TiO_2. The anomalous variation of band gap is attributed to the difference in strain content in the samples. These results are consistent with recent simulated results [33]. Yin et al. predicted a band gap reduction of ~0.25 eV for a stress of 8 GPa in anatase TiO_2 [33]. Interestingly, we found a band gap reduction of 0.43 eV for the T16 h sample as compared to the T0h, and it is reduced to 0.35 eV for T40 h sample. Our XRD analysis shows a maximum stress of ~0.6 GPa for the T16 h sample [see Table 2]. Thus, besides the strain effect, the effective reduction in band gap may partly be due to the oxygen vacancy defects that help in the band gap reduction. Interestingly, the PL results demonstrate the presence of oxygen vacancy states in different samples (see supporting information,

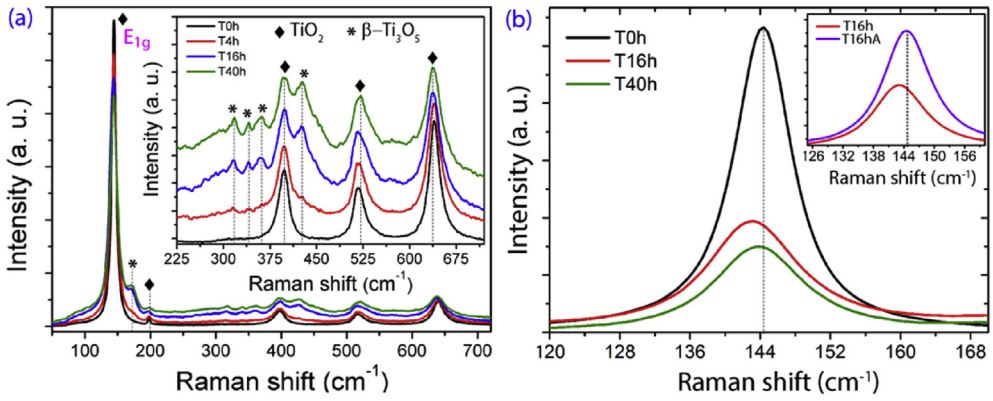

Fig. 7. (a) Raman spectra of T0h, T4 h, T16 h and T40 h samples. Inset show the enlarged view of the spectra in the range 225–700 cm^{-1}. Note that curves are vertically shifted for the clarity and vertical dotted line shows the peak shift. The "*" indicates the β-Ti_3O_5 phase and "◆" indicates the anatase phase of TiO_2. (b) Enlarged view of Raman shift for E_{1g} mode and the inset shows the shift in Raman peak for T16 h before and after annealing.

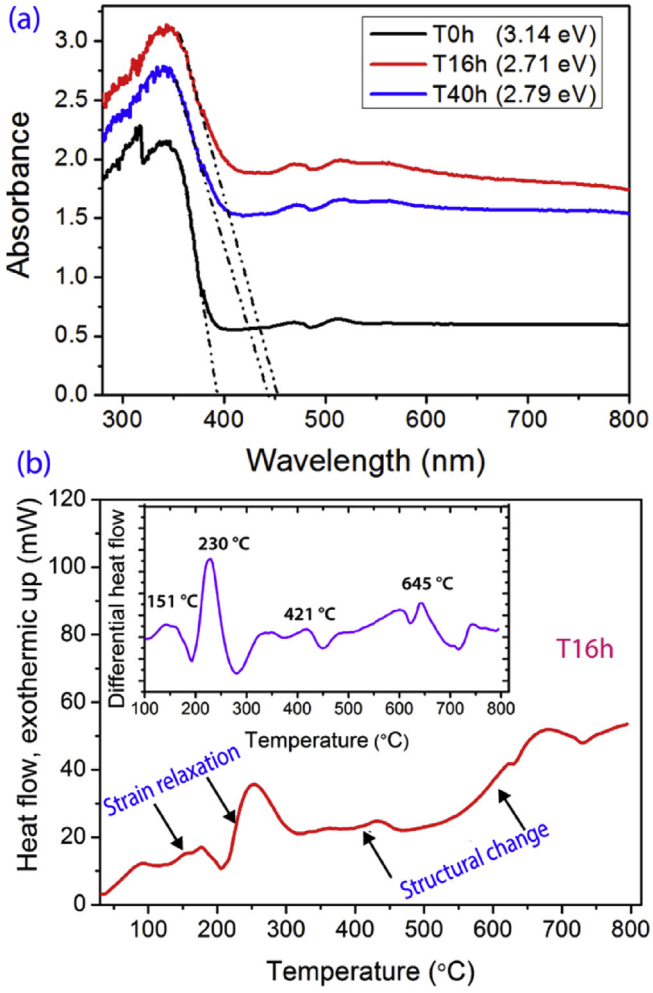

Fig. 8. (a) UV-vis absorption spectra (Kubelka–Munk function) of T0h, T16 h and T40 h samples extracted from DRS data. The band gap values are calculated from the intercept of the extrapolated lines. (b) DSC curve of T16 h sample. Inset shows the differentiated DSC curve and lower temperature peaks (151 and 230 °C) signify the strain relaxation and the higher temperature peaks (421 and 645 °C) reveal the structural changes.

Fig. S1). The defect concentration increases after milling. Oxygen vacancy mediated band gap modification has been reported for ZnO nanostructures [60]. It may be likely that the oxygen vacancy states appear near the band edge and with increasing oxygen vacancy concentration, the defect band causes an effective narrowing of band gap in TiO_2 NCs [42].

4.6. Strain relaxation and structural changes

In order to monitor the strain relaxation and structural change by heating, DSC measurements were performed on highly strained sample (T16 h) and results are shown in Fig. 8(b). The inset of Fig. 8(b) shows the differentiated curve of T16 h sample. The low temperature peaks at 151 and 230 °C clearly signify the strain relaxation during heat treatment [25]. Besides the strain relaxation, the structural changes may be expected in ball milled samples. The higher temperature DSC peak (645 °C) may be assigned to phase change from anatase to rutile without any ambiguity. Since anatase phase of TiO_2 is less stable at high temperature, it is converted to rutile upon heating. We have already discussed that at higher milling time a new phase β-Ti_3O_5 appears in the sample. The β-Ti_3O_5 further changes to α-Ti_3O_5 and then converted into λ-Ti_3O_5 at high temperature (1047 °C) [21,61]. β-Ti_3O_5 is an semiconducting phase with a nominal Ti^{3+}-$Ti^{3.33+}$-$Ti^{3.67+}$ electronic configuration of the three inequivalent Ti atoms in the monoclinic structure [62]. The phase transition have taken place due to the high pressure created during milling that caused structural rearrangement of the lattice topology leading to the formation of short Ti–Ti bonds in neighbouring edge-sharing TiO_6 octahedra. Liu and Shang showed from the energy calculation that β-Ti_3O_5 has a lower total energy and lower volume than the λ-Ti_3O_5 and this phase can form at higher pressure [61]. These results are consistent with our observation. The DSC peak at 421 °C is likely to be due to the phase change of β-Ti_3O_5 to α- Ti_3O_5. Note that λ-Ti_3O_5 and β -Ti_3O_5 can be identified from Raman spectroscopy [52]. In the present case, the Raman spectra confirm the presence of β-Ti_3O_5 phase in milled samples (Fig. 7(a)). The λ-Ti_3O_5 phase is stable at high temperature. Thus, the DSC results are fully consistent with the XRD and Raman analysis.

5. Conclusions

In conclusion, we have reported the growth of TiO_2 NCs of size down to ~11 nm using a simple ball-milling method and systematically investigated the strain evolution in TiO_2 NCs as a function of milling time. Besides the size reduction and non-monotonous evolution of strain, we have noticed the evolution of a new phase β-Ti_3O_5 from the Raman and XRD analyses, for the first time. The

broadening and shift of XRD peak positions are analysed with different models to understand the evolution of strain and particle size. The combined analysis of XRD and micro Raman spectra reveals that the 16 h milling gives rise to the highest tensile strain in TiO_2, and the strain reduces with further milling. The milling time appears to be the key factor controlling the size and strain of TiO_2 NCs. The most important observation for the ball milled TiO_2 NCs is the band gap reduction by tensile strain, reported for the first time. Our results demonstrated that the band gap narrowing in TiO_2 NCs is due to combined effect of lattice strain and lattice defects (mostly oxygen vacancies) induced by the milling. This is an important step for band gap tuning of semiconductor nanomaterials, which can be directly utilized in practical applications such as optoelectronics, photovoltaic and photocatalysis etc. Our visible light photocatalysis results on the ball milled TiO_2 NCs are promising. This simple fabrication also allows for production of large amount of materials for various commercial applications.

Acknowledgements

We acknowledge the CIF for the HRTEM and micro Raman facilities at IIT Guwahati. Thanks to Dr. Batakrushana Santara and Mr. Ramesh Ghosh for their suggestions. Thanks are due to Mr. Indrajit Talukdar for assistance in HRTEM measurements. We thank DEITY (Grant no. 5(9)/2012-NANO(VOL-II)) for the financial support.

Appendix A. Supplementary data

Supplementary data related to this article can be found at http://dx.doi.org/10.1016/j.jallcom.2016.03.154.

References

[1] M. Anpo, M. Takeuchi, J. Catal. 216 (2003) 505–516.
[2] A.F. Cipriano, C. Miller, H. Liu, J. Biomed. Nanotechnol. 10 (2014) 2977–3003.
[3] M. Grätzel, J. Sol-Gel Sci. Technol. 22 (2001) 7–13.
[4] W. Li, D. Corradini, M. Body, C. Legein, M. Salanne, J. Ma, K.W. Chapman, P.J. Chupas, A.-L. Rollet, C. Julien, K. Zhagib, M. Duttine, A. Demourgues, H. Groult, D. Dambournet, Chem. Mater. 27 (2015) 5014–5019.
[5] Y. Liu, J. Li, B. Zhou, H. Chen, Z. Wang, W. Cai, Chem. Commun. 47 (2011) 10314–10316.
[6] J. Medina-Valtierra, C. Frausto-Reyes, J. Ramírez-Ortiz, G. Camarillo-Martínez, Industrial Eng. Chem. Res. 48 (2009) 598–606.
[7] T. Ochiai, A. Fujishima, J. Photochem. Photobiol. C Photochem. Rev. 13 (2012) 247–262.
[8] J. Qiu, S. Zhang, H. Zhao, Sens. Actuat. B Chem. 160 (2011) 875–890.
[9] K.P.S. Zanoni, R.C. Amaral, N.Y. Murakami Iha, ACS Appl. Mater. Interfaces 6 (2014) 10421–10428.
[10] S. Ali Ansari, M. Mansoob Khan, M. Omaish Ansari, M. Hwan Cho, Ceram. Int. 41 (2015) 9131–9139.
[11] M. Farbod, M. Khademalrasool, Powder Technol. 214 (2011) 344–348.
[12] W. Li, C. Ni, H. Lin, C.P. Huang, S.I. Shah, J. Appl. Phys. 96 (2004) 6663–6668.
[13] X. Wei, R. Skomski, B. Balamurugan, Z.G. Sun, S. Ducharme, D.J. Sellmyer, J. Appl. Phys. 105 (2009) 07C517.
[14] T. Wang, H. Jiang, L. Wan, Q. Zhao, T. Jiang, B. Wang, S. Wang, Acta Biomater. 13 (2015) 354–363.
[15] S. Wu, Z. Weng, X. Liu, K.W.K. Yeung, P.K. Chu, Adv. Funct. Mater. 24 (2014) 5464–5481.
[16] X. Chen, S.S. Mao, Chem. Rev. 107 (2007) 2891–2959.
[17] T. Tong, A. Shereef, J. Wu, C.T.T. Binh, J.J. Kelly, J.-F. Gaillard, K.A. Gray, Environ. Sci. Technol. 47 (2013) 12486–12495.
[18] X. Li, W. Zheng, G. He, R. Zhao, D. Liu, ACS Sustain. Chem. Eng. 2 (2014) 288–295.
[19] N. Arimitsu, A. Nakajima, K. Saito, Y. Kameshima, K. Okada, Chem. Lett. 36 (2007) 106–107.
[20] L. Zheng, Sens. Actuat. B Chem. 94 (2003) 294–297.
[21] S.-i. Ohkoshi, Y. Tsunobuchi, T. Matsuda, K. Hashimoto, A. Namai, F. Hakoe, H. Tokoro, Nat. Chem. 2 (2010) 539–545.
[22] D. Reyes-Coronado, G. Rodríguez-Gattorno, M.E. Espinosa-Pesqueira, C. Cab, R.d. Coss, G. Oskam, Nanotechnology 19 (2008) 145605.
[23] H.Y. Zhu, Y. Lan, X.P. Gao, S.P. Ringer, Z.F. Zheng, D.Y. Song, J.C. Zhao, J. Am. Chem. Soc. 127 (2005) 6730–6736.
[24] S. Dhara, P.K. Giri, J. Nanosci. Nanotechnol. 11 (2011) 9215–9221.
[25] P. Giri, J. Phys. D Appl. Phys. 42 (2009) 245402–245408.
[26] P.K. Giri, S. Bhattacharyya, Dilip K. Singh, R. Kesavamoorthy, B.K. Panigrahi, K.G.M. Nair, J. Appl. Phys. 102 (2007) 093515.
[27] A. Khorsand Zak, W.H. Abd Majid, M.E. Abrishami, R. Yousefi, Solid State Sci. 13 (2011) 251–256.
[28] V. Mote, Y. Purushotham, B. Dole, J. Theor. Appl. Phys. 6 (2012) 6.
[29] B. Choudhury, A. Choudhury, Int. Nano Lett. 3 (2013) 55.
[30] S.A. Ansari, M.M. Khan, M.O. Ansari, M.H. Cho, Sol. Energy Mater. Sol. Cells 141 (2015) 162–170.
[31] S.A. Ansari, M.M. Khan, M.O. Ansari, M.H. Cho, New J. Chem. 39 (2015) 4708–4715.
[32] A.K. Tripathi, M.K. Singh, M.C. Mathpal, S.K. Mishra, A. Agarwal, J. Alloys Compd. 549 (2013) 114–120.
[33] W.-J. Yin, S. Chen, J.-H. Yang, X.-G. Gong, Y. Yan, S.-H. Wei, Appl. Phys. Lett. 96 (2010) 221901.
[34] D.V. Potapenko, Z. Li, J.W. Kysar, R.M. Osgood, Nano Lett. 14 (2014) 6185–6189.
[35] C. Suryanarayana, Mechanical Alloying and Milling, CRC Press, 2004, pp. 83–94.
[36] Cullity BD, Elements of X-Ray Diffraction, Pearson (2001).
[37] D. Balzar, H. Ledbetter, J. Appl. Crystallogr. 26 (1993) 97–103.
[38] B.E. Warren, B.L. Averbach, J. Appl. Phys. 21 (1950) 595–599.
[39] H. Rietveld, Acta Crystallogr. 22 (1967) 151–152.
[40] R.M.Y. Thakur Prasad Yadav, Dinesh Pratap Singh, Nanosci. Nanotechnol. 2 (2012) 22–48.
[41] V. Sepelak, S. Begin-Colin, G. Le Caer, Dalton Trans. 41 (2012) 11927–11948.
[42] B. Santara, P.K. Giri, K. Imakita, M. Fujii, Nanoscale 5 (2013) 5476–5488.
[43] D.H. Hanaor, C. Sorrell, J. Mater. Sci. 46 (2011) 855–874.
[44] M. Birkholz, Wiley-VCH Verlog GmbH and Co KGaA, Weinheim, (2006).
[45] J.-M. Zhang, Y. Zhang, K.-W. Xu, V. Ji, Chin. Phys. B 17 (2008) 1565–1573.
[46] L. Borgese, E. Bontempi, M. Gelfi, L.E. Depero, P. Goudeau, G. Geandier, D. Thiaudière, Acta Mater. 59 (2011) 2891–2900.
[47] W.F. Zhang, Y.L. He, M.S. Zhang, Z. Yin, Q. Chen, J. Phys. D Appl. Phys. 33 (2000) 912.
[48] S. Kelly, F.H. Pollak, M. Tomkiewicz, J. Phys. Chem. B 101 (1997) 2730–2734.
[49] M.J. Seepanovic, M.U. Grujie-Brojcin, Z.D. Dohcevie-Mitrovie, Z.V. Popovie, Mater. Sci. Forum. 518 (2006) 101–106.
[50] F. Tian, Y. Zhang, J. Zhang, C. Pan, J. Phys. Chem. C 116 (2012) 7515–7519.
[51] Y. Wu, Q. Zhang, X. Wu, S. Qin, J. Liu, J. Solid State Chem. 192 (2012) 356–359.
[52] A. Ould-Hamouda, H. Tokoro, S.I. Ohkoshi, E. Freysz, Chem. Phys. Lett. 608 (2014) 106–112.
[53] D. Georgescu, L. Baia, O. Ersen, M. Baia, S. Simon, J. Raman Spectrosc. 43 (2012) 876–883.
[54] A. Li Bassi, D. Cattaneo, V. Russo, C.E. Bottani, E. Barborini, T. Mazza, P. Piseri, P. Milani, F.O. Ernst, K. Wegner, S.E. Pratsinis, J. Appl. Phys. 98 (2005) 074305.
[55] S. Sahoo, A.K. Arora, V. Sridharan, J. Phys. Chem. C 113 (2009) 16927–16933.
[56] D. Bersani, P.P. Lottici, X.-Z. Ding, Appl. Phys. Lett. 72 (1998) 73–75.
[57] J. Chen, G. Conache, M.-E. Pistol, S.M. Gray, M.T. Borgström, H. Xu, H.Q. Xu, L. Samuelson, U. Håkanson, Nano Lett. 10 (2010) 1280–1286.
[58] R.W. Meulenberg, T. Jennings, G.F. Strouse, Phys. Rev. B 70 (2004) 235311.
[59] I. Zardo, S. Conesa-Boj, F. Peiro, J.R. Morante, J. Arbiol, E. Uccelli, G. Abstreiter, Fontcuberta i Morral, Phys. Rev. B 80 (2009) 245324.
[60] S.A. Ansari, M.M. Khan, S. Kalathil, A. Nisar, J. Lee, M.H. Cho, Nanoscale 5 (2013) 9238–9246.
[61] L. Rui, S. Jia-Xiang, Model. Simul. Mater. Sci. Eng. 20 (2012) 035020.
[62] R. Makiura, Y. Takabayashi, A.N. Fitch, H. Tokoro, S.-i. Ohkoshih, K. Prassides, Chem. – An Asian J. 6 (2011) 1886–1890.